On-line clearing and staining method for the efficient optical imaging of large volume samples at the cellular resolution

YUNFEI ZHANG,[1] GUANGCAI LIU,[1] XIANGNING LI,[1,2,3] HUI GONG,[1,2] QINGMING LUO,[1,2,3] AND XIAOQUAN YANG[1,2,*]

[1]*Britton Chance Center for Biomedical Photonics, Wuhan National Laboratory for Optoelectronics, MoE Key Laboratory for Biomedical Photonics, Huazhong University of Science and Technology, Wuhan 430074, China*
[2]*HUST-Suzhou Institute for Brainsmatics, JITRI, Suzhou, 215123, China*
[3]*Key Laboratory of Biomedical Engineering of Hainan Province, School of Biomedical Engineering, Hainan University, Haikou, China*
[*]*xqyang@mail.hust.edu.cn*

Abstract: Optical microscopy is a powerful tool for exploring the structure and function of organisms. However, the three-dimensional (3D) imaging of large volume samples is time-consuming and difficult. In this manuscript, we described an on-line clearing and staining method for efficient imaging of large volume samples at the cellular resolution. The optimized cocktail can increase staining and imaging depth to reduce the sectioning and scanning time, more than doubling the operational efficiency of the system. Using this method, we demonstrated the rapid acquisition of Aβ plaques in whole mouse brain and obtained a complete set of cytoarchitecture images of an adult porcine hemisphere at $1.625 \times 1.625 \times 10 \ \mu m^3$ voxel resolution for about 49 hours.

1. Introduction

Brain is one of the most important and complex organs of the humans. It has complex structures and billions of neurons [1,2]. The brain structure is still urgently needed for neuroscientists [3]. Therefore, it is very meaningful to develop whole brain imaging platforms for mapping brain atlas and neural circuits [4,5]. Optical clearing technology combined with light-sheet microscopy [6] for obtaining whole mouse brain images has been used widely, such as Scale [7], SeeDB [8], 3DISCO [9], CLARITY [10], CUBIC [11], FRUIT [12], PEGASOS [13], MACS [14], and their variants [15,16]. In recent years, the optical clearing technology for large samples such as mouse whole-body and human organ has also developed [17,18]. But these methods require several months for processing samples. With the increasing of volume, the samples become more and more difficult to be cleared and stained. Due to the limited working distance of the objective with large numerical aperture, high-resolution imaging range can also be difficult to cover the whole organ if we use light-sheet microscopy.

   Alternating operation of physical sectioning and optical sectioning microscopy [19] can realize high resolution 3D imaging for whole brain [20–23]. Physical sectioning can expand imaging depth and the imaging range of the system that is only limited by the moving stage. Combining physical sectioning and optical microscopy has the potential to acquire high resolution images of large volume samples. However, continuous ultrathin sectioning is time-consuming and seriously slows down the process of obtaining data. For example, in the wide-field large-volume tomography (WVT) system [24], the exposure time of the scientific complementary metal-oxide semiconductor (sCMOS) camera only accounts for 30% of the total imaging time. A large amount of time is consumed in sectioning and stage movement. Using the existing parameters

and modes of the WVT system, imaging a macaque brain requires the system to continuously run for nearly one year.

The concept of on-line clearing was proposed for imaging mouse brain by adding clearing reagent to the water tank, expanding the imaging depth and reducing the number of sectioning [25]. However, this method uses high concentrations of fructose and urea as transparent reagents, and crystal precipitation may occur during long-term imaging of large volume samples. Viscosity up to 36 mPa.s can also hinder the vibration of the blade, thereby affecting the surface flatness of the sample. In addition, the reagent is not compatible with hydrophilic fluorescent dyes due to its low water ratio. But large volume animal research often relies on chemical fluorescent dyes for specific structural labeling because of the long-time and difficult process of establishing transgenic models [26,27].

To overcome the above shortcomings and extend the concept to wider application, we proposed an on-line clearing and staining method for imaging large volume samples at cellular resolution. We optimized the clearing reagent by introducing the dimethyl sulfoxide (DMSO), a kind of penetration enhancer to enhance clearing ability and keep low viscosity. We achieved rapid on-line staining by adding fluorescent dye to the clearing reagent. We evaluated performance of the reagent on clearing efficiency, compatibility with various fluorophores, staining efficiency, and sample deformation. Using our method, we showed that Aβ plaques distribution in the whole mouse brain and cytoarchitecture of adult porcine hemisphere at cellular resolution could be obtained. This method makes it possible to image the large volume samples in high speed, which greatly paves the way for exploring a variety of organs from large animal models.

2. Materials and methods

2.1. Animals

This study used three 3-month-old C57BL/6J, Thy1-GFP, and VIP-ires-Cre; Ai14 mice, two 6-month-old 5×FAD mice. (Jackson Laboratory, Bar Harbor, ME, USA). All animal experiments were performed according to procedures approved by the Institutional Animal Ethics Committee of Huazhong University of Science and Technology. The porcine brain was retrieved after death from an adult pig used for food production.

2.2. Agarose embedding

The brain tissues are immersed in 4% paraformaldehyde (PFA, Sigma-Aldrich, USA) to preserve and fix for 5-7 days. Before the experiment, the fixed brain is immersed in the clearing reagent that consist of 30% (wt vol^{-1}) fructose (Aladdin, China), 20% (wt vol^{-1}) urea (Aladdin, China), and 20% (wt vol^{-1}) DMSO (Aladdin, China) for 4 days for pretreatment, and then placed in the mold filled with 5% agarose (Sigma-Aldrich, USA) solution. The mold is placed in a 55 °C water bath. The brain contacts with the agarose solution and cross link for at least 30 min. Then the mold is taken out and free cooling for 30 min. After that, the embedded brain tissue is taken out from the mold and immersed in the clearing reagent for storage or conducted experiments directly [28].

2.3. On-line clearing and staining method

In order to quickly obtain three-dimensional (3D) data of large volume samples, we chose the line confocal imaging method [29] and optimized the imaging solution to realize on-line clearing and staining during imaging. A schematic diagram of on-line clearing and staining system for imaging large volume sample is shown in Fig. 1(a). Line illumination is combined with a high-precision 3D stage to complete the scanning of the entire sample surface, and a vibration slicer is used to expand the imaging depth. In order to quickly obtain 3D images with cellular resolution of large volume samples, the system has installed a 4×, NA = 0.28 objective (Olympus, Japan) with

10 µm axial scanning step. The image voxel resolution is $1.625 \times 1.625 \times 10$ µm^3. The large volume sample embedded in agarose is immersed in the on-line clearing and staining imaging solution, and tens of micrometers thickness of sample beneath the surface is cleared and stained during the sectioning and imaging process. To illustrate the mechanism of interaction between sample and imaging solution, the schematic diagram is further shown in Fig. 1(b). During the tissue sectioning, the newly exposed sample surface comes into contact with the imaging solution. The tissue fluid and water are rapidly replaced by the high concentration and high refraction immersion solution. The refractive index of the sample surface becomes homogeneous. At the same time, small molecular fluorescent dyes are transported into the tissue to mark the target substance. Thanks to the increase in staining depth and imaging depth, the physical sectioning thickness of the sample can be increased. So the total number of sectioning and data acquisition time will be reduced.
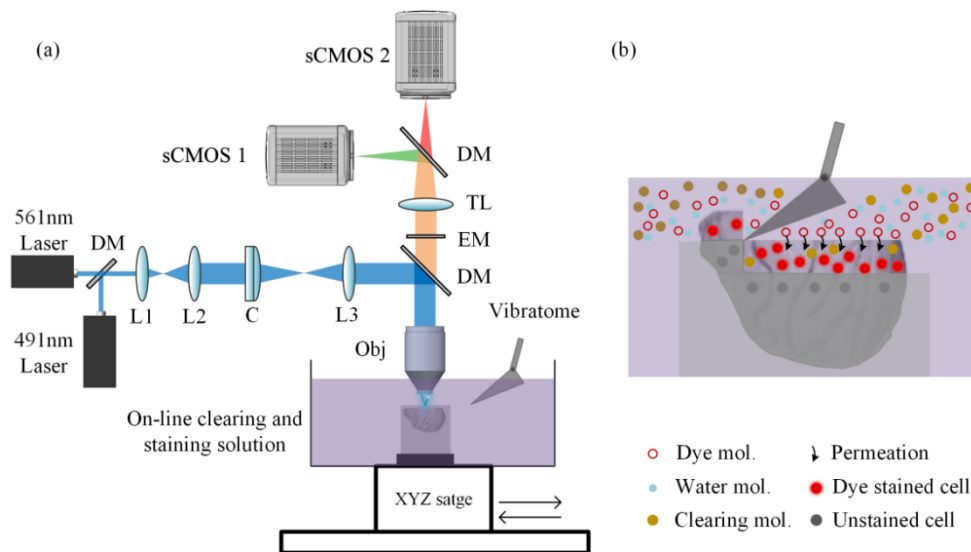

Fig. 1. Principle of on-line clearing and staining method. (a) Schematic of the imaging system for obtaining dual channel data of large volume samples. DM, dichroic mirror; L1-3, lens; C, cylindrical lens; OBJ, objective lens; EM, emission filter; TL, tube lens. (b) Schematic of on-line clearing and staining during sectioning.

A suitable imaging solution is crucial for achieving on-line clearing and staining of large volume samples, thereby accelerating data acquisition. First, the imaging solution needs to be able to quickly realize optical clearing of samples surface. Second, a lower viscosity is required to avoid obstructing sectioning and crystal precipitation. At present, various clearing reagents that have been reported cannot directly meet the demand. We have screened and optimized the imaging solution.

2.4. Clearing reagent based on a permeation enhancer

Inspired by various hydrophilic clearing methods [7,12], we use fructose and urea as the basic components in the reagents. Considering the viscosity of the solution, the fructose concentration is set at 30% (wt vol^{-1}) and the urea concentration is set at 20% (wt vol^{-1}). In order to enhance clearing ability and speed, we compared the clearing rate of three penetration enhancers added to the basic clearing solution [30,31], as show in Fig. 2(a). Three penetration enhancers are 1,2-propanediol (aladdin, China), 1,3-Dimethyl-2-iminazolidinone (DMI, aladdin, China) and Dimethyl sulfoxide (DMSO,aladdin, China), set at 20% (wt vol^{-1}). We used a vibratome to
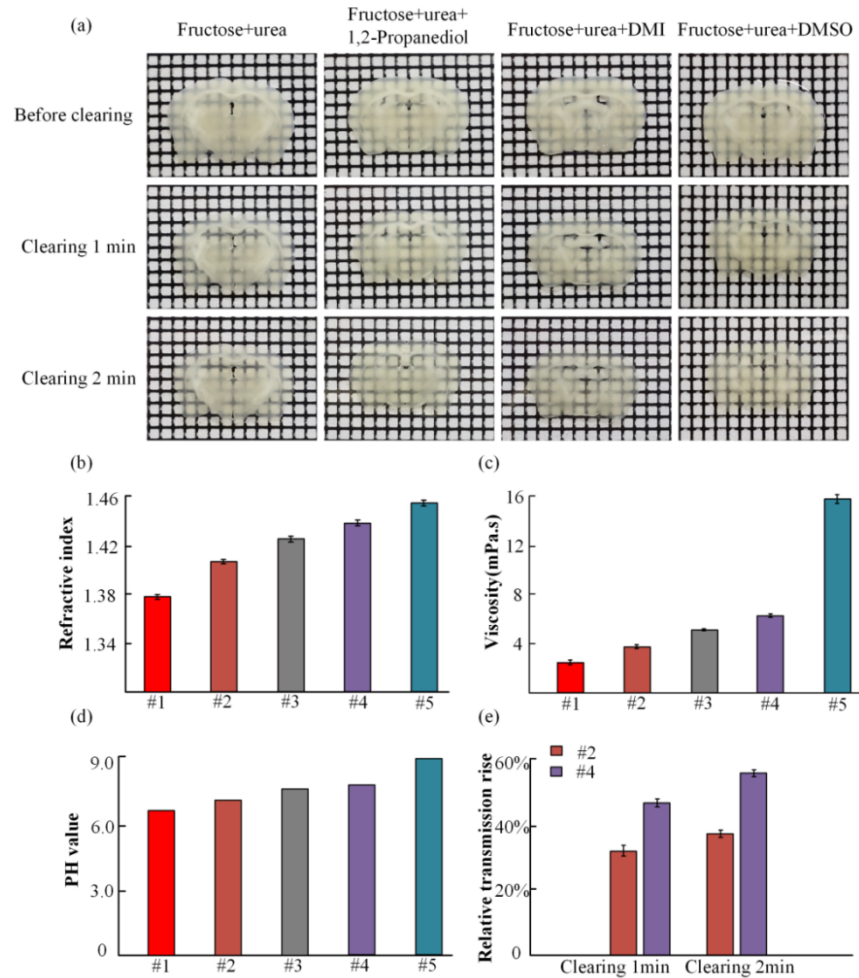
Fig. 2. Screening of penetration enhancers and measurement of reagent parameters. (a) Comparing the rapid clearing ability of different reagents. Brain slices are placed on the 1 mm grid to image before and after clearing for 1 min and 2 min. The clearing reagent components from left to right are 30% (wt vol^{-1}) fructose + 20% (wt vol^{-1}) urea, 30% (wt vol^{-1}) fructose + 20% (wt vol^{-1}) urea + 20% (wt vol^{-1}) 1,2-propanediol, 30% (wt vol^{-1}) fructose + 20% (wt vol^{-1}) urea + 20% (wt vol^{-1}) DMI, and 30% (wt vol^{-1}) fructose + 20% (wt vol^{-1}) urea + 20% (wt vol^{-1}) DMSO. (b) - (d) Measured refractive index, viscosity, and pH of different reagents. #1, 30% (wt vol^{-1}) fructose; #2, 30% (wt vol^{-1}) fructose + 20% (wt vol^{-1}) urea; #3, 30% (wt vol^{-1}) fructose + 20% (wt vol^{-1}) urea + 10% (wt vol^{-1}) DMSO; #4, 30% (wt vol^{-1}) fructose + 20% (wt vol^{-1}) urea + 20% (wt vol^{-1}) DMSO; #5, 30% (wt vol^{-1}) fructose + 20% (wt vol^{-1}) urea + 30% (wt vol^{-1}) DMSO. (e) The relative transmission rise of a 100 µm brain slice before and after clearing for 1 min and 2 min using #2 and #4.

slice the mouse brain into 300 μm-thick sections and took photos to record transparency of brain sections before and after clearing. We found that the clearing speed of combination reagent of fructose, urea, and DMSO was superior to others, as shown in Fig. 2(a). In order to further determine the formula of the clearing reagent and the optimal concentration of DMSO, we measured the viscosity (NDJ-5S, LICHEN, China), refractive index (WAY-2W, Shanghai YiCe Apparatus & Equipment Co., China), and pH (pH-100, LICHEN, China) of five different combinations of reagents, as shown in Fig. 2(b) - (d).

The refractive index of lipids, proteins, and other substances in the sample are generally 1.4-1.5. High refractive index solutions are more conducive to match and achieve better optical clearing [32]. As the concentration of DMSO increases, the refractive index of the reagent continues to increase, which means that the clearing ability of the reagent continues to improve, but the viscosity also increases accordingly. When the concentration of DMSO in the reagent reaches 30% (wt vol^{-1}), the viscosity of the solution suddenly increases to 16.77 mPa.s. In order to balance clearing ability and viscosity, we ultimately selected 20% (wt vol^{-1}) DMSO as a penetration enhancer to add to the reagent. The refractive index of the reagent reaches 1.44 and its viscosity is 6.67 mPa.s. Alkaline reagents are also more likely to maintain the fluorescence signal in the sample [33]. To quantitatively demonstrate the effectiveness of DMSO, we used an Optical power meter (Nova II, Ophir Optronics, Israel) and a laser (491 nm, Cobolt, Solna, Sweden) to measure the intensity change and calculated optical transmission rate of a 100 μm brain slice before and after clearing. As shown in Fig. 2(e), clearing brain slices with 30% (wt vol^{-1}) fructose and 20% (wt vol^{-1}) urea reagent for 1 min and 2 min, the light transmission rise by 32.6% and 38.1%, respectively. Using 30% (wt vol^{-1}) fructose, 20% (wt vol^{-1}) urea, and 20% (wt vol^{-1}) DMSO, the light transmission rise by 47.8% and 57.1%, respectively. So we selected 30% (wt vol^{-1}) fructose + 20% (wt vol^{-1}) urea + 20% (wt vol^{-1}) DMSO as our clearing reagent. All solutes are dissolved in distilled water and can remain stable for several months.

3. Results

3.1. Fluorescence preservation of the clearing reagent

We performed 100 μm sectioning of fluorescent labeled mouse brain, soaked them in 0.01 M phosphate-buffered saline (PBS, Sigma-Aldrich, USA) solution, and then imaged them using our imaging system. Subsequently, we transferred the brain slices to the clearing reagent, imaged them after 2 min. As shown in Fig. 3, we compared the performance of various fluorescent signals before and after clearing for 2 min including GFP, tdTomato, PI, and TH-S signals. As a representative, GFP was monitored for a long time, and no fluorescence quenching was observed during prolonged contact with the clearing reagent. On the contrary, due to the clearing and uniform refractive index of the sample, more fluorescence signals are detected.

3.2. Imaging depth of on-line clearing and staining

We placed the whole mouse brain in the water tank, filled up the imaging solution, and performed a deep scan of the sample in 10 μm axial step using our imaging system. By viewing the images, we can measure the imaging depth of the proposed clearing reagent for mouse brain. As shown in the Fig. 4(a) and (b), the GFP labeled mouse brain images are displayed at intervals of 20 μm before and after clearing, respectively. Before clearing, the image quality of the mouse brain on the surface layer is good, but as the depth increases, the image quality rapidly deteriorates, and the collected signals gradually weaken. The cleared sample has the property of being transparent to light, and the imaging depth is greatly expanded. Soma and fiber signals can still be detected at 100 μm. We evaluated image quality by calculating the root mean square (RMS) of the image and obtained the corresponding normalized RMS curve with increasing imaging depth by polynomial fitting, as shown in Fig. 4(c). When the imaging depth reaches 100 μm, the RMS of the image
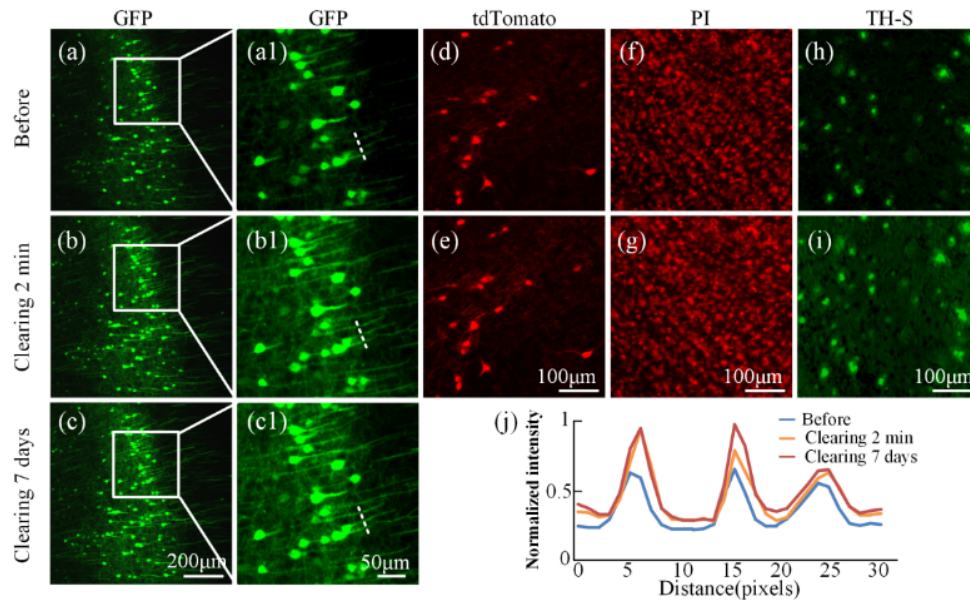
Fig. 3. Compatibility of reagents with fluorescent proteins. (a)-(c) The GFP mouse brain slice images before clearing, clearing 2 min and clearing 7 days. (a1)-(c1) The enlarged view of the white box in (a)-(c). (d) and (e) Images of tdTomato labeled mouse brain slice before and after 2 min clearing. (f) and (g) Images of mouse brain slice stained with PI before and after 2 min clearing. (h) and (i) Images of mouse brain slice labeled with TH-S before and after 2 min clearing. (j) The normalized intensity curve at the white dotted line of (a1)-(c1).

can be maintained at 80% of the surface layer. In order to validate staining efficiency, we added PI (Sigma-Aldrich, USA) or TH-S (Sigma-Aldrich, USA) to the clearing reagent to form the final online clearing and staining reagent. The concentration of PI is 2µg/ml in the solution. The imaging depth of the brain after PI staining was measured, and the results are shown in Fig. 4(d)-(f). From the Fig. 4(d), cells can be seen at $60\,\mu m$. While in the Fig. 4(e), the contrast in the image deteriorates at $20\,\mu m$, making it difficult for cells to be recognized. Combining online clearing and staining method, the imaging depth of PI staining can be expanded obviously. Similarly, the concentration of TH-S is 0.25% (wt vol^{-1}) in the solution. The imaging depth of the brain after TH-S staining was measured, and the results are shown in Fig. 4(g)-(i). TH-S, combined with the clearing reagent, is easier to reach the depths of the sample to label the Aβ plaques. Meanwhile, as the sample becomes transparent, we can detect deeper signals.

3.3. Sample deformation of on-line clearing and staining

Deformation is inevitable during the process of sample clearing. In order to evaluate the impact of our proposed reagent on sample volume, micro-computed tomography (micro-CT) was used to scan and image an adult porcine brain. The collected images were processed and imported into Amira software (v 5.3.2, FEI, France) for 3D reconstruction and volume calculation to obtain the volume of the sample before clearing. Then the porcine brain was immersed in the reagent and scanned every 2 days. The volume data of porcine brain changes with clearing time is shown in the Fig. 5. When the sample just contacts with the reagent, the volume of the sample will decrease in a certain proportion due to dehydration. On the fourth day, the sample deformation reaches balance. The volume of the sample basically remains unchanged. Therefore, in subsequent experiments and imaging processes, a sample pretreatment stage was added to reduce the deformation of the sample during the imaging process. The steps of pretreatment are
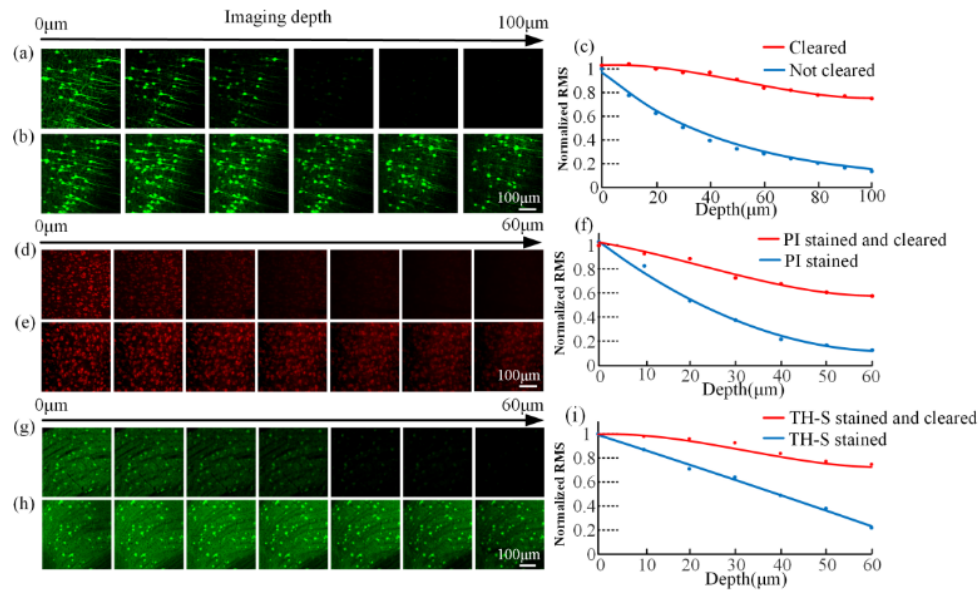
Fig. 4. Imaging depth before and after on-line cleaning and staining. (a) and (b) The GFP labeled mouse brain images before and after clearing for 2 min at intervals of 20 μm. (c) The correlation curve of RMS and imaging depth by polynomial fitting for GFP-labeled brain. (d) and (e) The PI stained mouse brain images before and after clearing and staining for 2 min at intervals of 10 μm. (f) The correlation curve of RMS and imaging depth by polynomial fitting for PI-stained brain. (g) and (h) The TH-S stained mouse brain images before and after clearing and staining for 2 min at intervals of 10 μm. (f) The correlation curve of RMS and imaging depth by polynomial fitting for TH-S stained brain.

as follows: Immerse the fixed sample in the clearing solution for at least 4 days; Take out the sample and directly embed it in agarose; Place the embedded sample in a water tank containing the on-line clearing and staining solution for imaging.

In fact, the obvious sample deformation mainly occurs in the physical sectioning position. In order to quantitatively analyze the sample deformation obtained using our method, we imaged a porcine brain with 50 μm imaging depth and 40 μm sectioning thickness. The 10 μm redundant information was used for data registration. We used the Descriptor based registration plugin [34] in ImageJ software to detect the transformation of the two layers of images before and after physical sectioning. The RegularizeData3D function in MATLAB R2017a (License No. 40588452) was used to interpolate and fit the obtained transformation data at each position, and output the porcine brain deformation map, which includes deformation in the X and Y direction, as shown in the Fig. 5(d) and (e). Due to the low axial resolution of the imaging system, no significant deformation observed in the Z direction. In fact, the image shifting obtained using our system are actually only a few pixels, and the impact on the study of cells with a diameter of tens of micrometers is negligible.

3.4. Whole brain Aβ plaque acquisition

Aβ plaque is one of the pathological features of Alzheimer's disease. Visualizing the distribution of plaques in the whole brain is extremely important for research on the spatiotemporal origin and development of Alzheimer's disease [35]. TH-S is a type of fluorescence dye that can specifically bind to Aβ plaques [36]. We added the TH-S to on-line clearing reagent forming the on-line clearing and staining reagent to acquire the Aβ plaques images quickly.
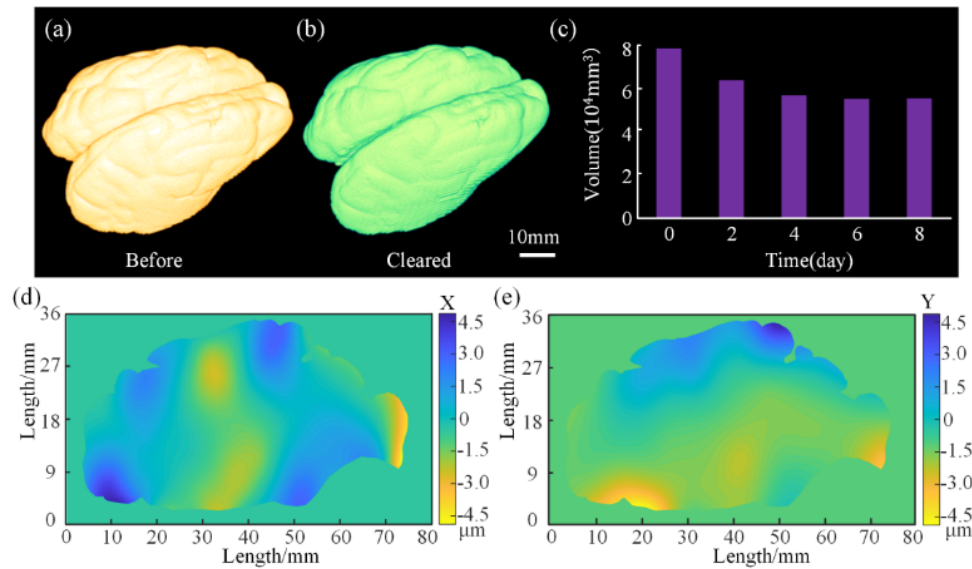
Fig. 5. Evaluation of sample deformation. (a) and (b) 3D reconstruction of porcine brain before and after clearing 4 days. (c) A histogram of porcine brain volume with clearing time. (d) and (e) X-direction (physical sectioning direction, corresponding anterior-posterior axis) and Y-direction (corresponding dorsal-ventral axis) deformation from the upper layer to the next layer before and after sectioning, respectively.

To verify the specificity of on-line TH-S staining, we used a vibratome to slice the 5×FAD mouse brain into $70\,\mu m$ thick sections and performed immunofluorescence staining and imaging on the mouse brain slices. The mouse monoclonal antibody MOAB-2 diluted at 1:800 (Biosensis, M-1586-100) was used to combine amyloid beta peptide and the secondary antibody is Goat Anti-Mouse Alexa Fluor@405 diluted at 1:1000 (Abcam, ab175660). The subsequent operation and other related reagents are consistent with the conventional protocols [37]. The on-line clearing and TH-S staining reagent with 30% (wt vol^{-1}) fructose + 20% (wt vol^{-1}) urea + 20% (wt vol^{-1}) DMSO + 0.25% (wt vol^{-1}) TH-S stained the mouse brain slices for 2 min without washing, simulating the actual on-line clearing and staining process. Finally, we imaged the brain slice using a commercial confocal microscope (Zeiss LSM710; 10×, NA0.5) and compared the results of the same brain slice stained with TH-S and immunofluorescence staining using MOAB-2 antibody, as shown in the Fig. 6(a) and (b). The white arrows in enlarged images showed the Aβ plaques co-labeling of TH-S and MOAB-2 staining. To obtain the distribution of Aβ plaques in the whole brain, we used on-line clearing and TH-S staining reagent as imaging solution to imaging the whole brain. In this experiment, the physical sectioning thickness was set to $40\,\mu m$ and imaging depth was set to $50\,\mu m$ with $5\,\mu m$ axial interval. In order to reduce light absorption by the dark color imaging solution, we used the 20X objective lens (UPLSAPO 20XO, Olympus, Japan) with $270\,\mu m$ working distance. we obtained whole brain data through mosaic stitching imaging method. As shown in the Fig. 6(c), the brain contour can be obtained by reconstruction of the whole brain images using the Amira software. The distribution of Aβ plaques at different coronal slices is showed in Fig. 6(d)-(m). The distribution of Aβ plaques in thalamus and hippocampus is further magnified and shown in Fig. 6(h1) and (i1). We can also display and study the 3D spatial position relationship between Aβ plaques, as shown in Fig. 6(i2) and (i3).
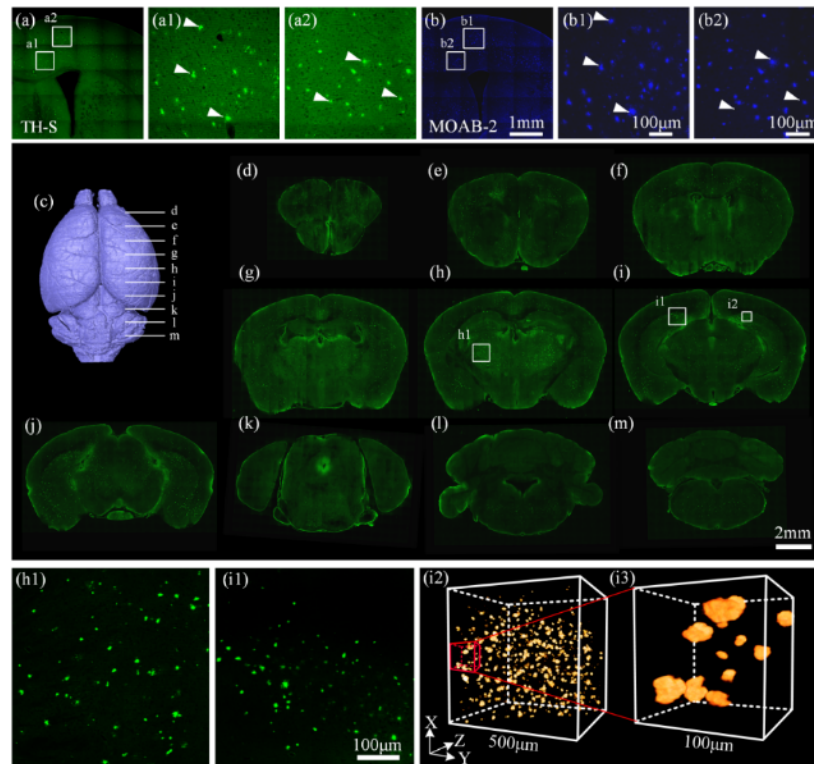
Fig. 6. Aβ plaques distribution in the whole mouse brain. (a) and (b) The brain slice images stained by TH-S and MOAB-2, respectively. (a1), (a2), (b1), and (b2) The enlarged views of the white box in the (a) and (b). The white arrows indicate the co-labeling results of TH-S and MOAB-2. (c) The contour of a 6-month-old 5×FAD mouse brain. (d)–(m) The coronal slices of the mouse brain at the corresponding positions of the white line at the (c), respectively. The coronal slices are displayed at an interval of 1 mm. (h1) The enlarged view of the white box in the (h), showing the distribution of Aβ plaques in the thalamus. (i1) The enlarged view of the white box in the (i), showing the distribution of Aβ plaques in the hippocampus. (i2) A data cube displaying the 3D distribution of Aβ plaques. (i3) The enlarged view of the red cube in (i2) shows the plaque morphology at cellular resolution.

3.5. Porcine hemisphere cytoarchitecture

Cytoarchitecture data is the foundation for drawing brain atlas and structural localization [38]. We can utilize the proposed on-line clearing and staining system to quickly obtain 3D images of large volume samples. As shown in the Fig. 7, We conducted on-line clearing and PI staining for imaging of an adult porcine hemisphere. To ensure image quality, the physical sectioning at 40 μm step and line-scanning imaging at 10 μm step and 50 μm imaging depth alternately for about 2 days to complete the imaging. Our system allowed the porcine brain to be cleared, stained and imaged layer by layer. We used the MATLAB software to stitch images and remove the artifacts in a T7600 workstation (two Intel E5-2687w CPUs, 256GB memory and a Nvidia K6000 graphics card, Dell Inc., USA). The 3D reconstruction and visualization are realized by Amria software. Because of the 3D imaging, horizontal plane, coronal plane and sagittal plane images can also be visualized in the same set of data, as shown in the Fig. 7(c)-(e). In order to demonstrate that our method can achieve uniform PI staining of large volume samples, enlarged images of different positions in a typical porcine brain image are shown in Fig. 7(f)-(m). The further enlarged views, as shown in the Fig. 7(i1) and (m1), indicate the cellular resolution images.
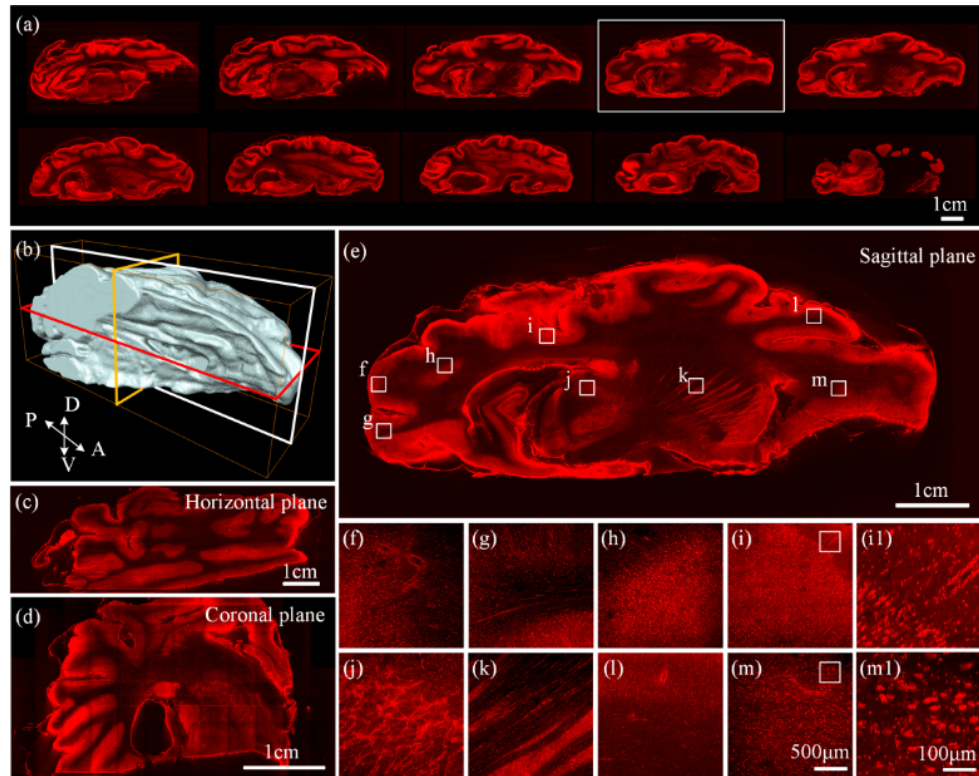
Fig. 7. A complete cytoarchitecture data set for an adult porcine hemisphere. (a) The porcine brain sagittal plane images displayed at interval of 2 mm. (b) The outline of a porcine hemisphere. (c) The typical horizontal plane image located in the red box of the (b). (d) The typical coronal plane image located in the yellow box of the (b). (e) The typical sagittal plane image located in the white box of the (a) and (b). (f)-(m) The enlarged views of white box in the (e). (i1) and (m1) The enlarged view of white box in the (i) and (m).

Due to the clearing and staining of samples with a thickness of several tens of micrometers during the imaging process, it has been verified that the imaging depth is increased, and the

thickness of the sectioning can be increased several times, greatly reducing the total number of physical sectioning. In addition, the mechanical movement of the sample from the imaging position to the sectioning position is also reduced. We compared in detail the data acquisition time with or without on-line clearing and staining at voxel resolution $1.625 \times 1.625 \times 10$ μm^3. The imaging depth and sectioning thickness are both 10 μm in conventional system. In on-line clearing and staining system, the imaging depth is 40 μm with 10 μm axial scanning interval, and the sectioning thickness is 50 μm. As shown in Fig. 8, the first bar for each histogram is the time using conventional line scan and vibratome system, consisting of three parts: imaging time, stage movement time, and physical sectioning time. The second bar is the total time using the on-line clearing and staining method. Due to the redundant data, the imaging time has slightly increased, but the time for physical sectioning and stage movement in both sectioning and imaging positions has significantly decreased. In the mouse whole brain (size: $14 \times 10 \times 10$ mm^3) imaging, the total time using or not using on-line clearing and staining is 2.63 h and 8.76 h, respectively. In the porcine hemisphere (size: $80 \times 36 \times 25$ mm^3) imaging, the total time using or not using on-line clearing and staining is 49.15 h and 132.79 h, respectively. By calculating, we can conclude that using on-line clearing and staining can more than double the speed for obtaining 3D data of the system.
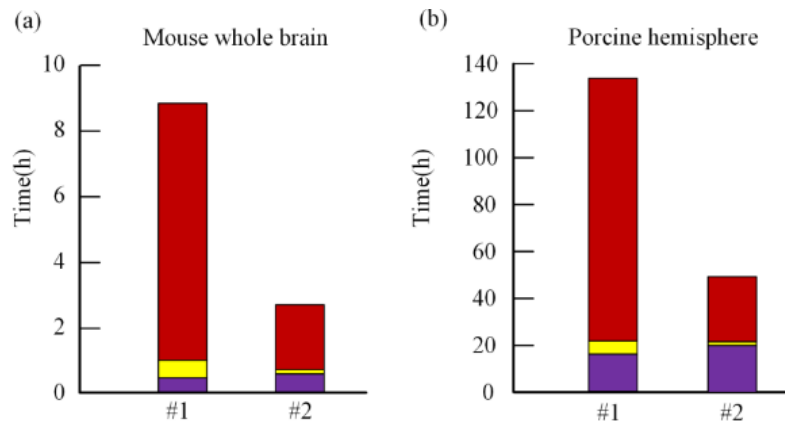
Fig. 8. Time comparison. (a)-(c) The total time for obtaining data using conventional line scan and vibratome system (#1) and on-line clearing and staining system (#2). The total time includes imaging time (purple), stage movement time (yellow), and physical sectioning time (red).

4. Discussion and conclusion

Optical clearing technology combined with light-sheet microscopy is a widely used 3D imaging method. However, with the increase of sample volume, traditional methods such as tissue optical clearing and fluorescent staining are difficult to realize. We often spend months preparing samples for imaging. The imaging range of a light-sheet microscopy needs to be balanced with imaging resolution. Physical sectioning can infinitely expand the imaging depth to realize large volume sample imaging with various optical microscopy. But physical sectioning requires a lot of time. Long term data collection will affect the cycle of biological research and analysis.

In order to reduce the sectioning and stage movement time of the system, we optimized the imaging solution to clear and stain the sample surface during the sectioning and imaging processes. Imaging solutions with clearing and staining need to meet the characteristics of high refractive index and low viscosity. We measured the various parameters of the reagent and ultimately determined the optimal clearing solution that is 30% (wt vol^{-1}) fructose + 20% (wt

vol^{-1}) urea + 20% (wt vol^{-1}) DMSO. TH-S and PI with appropriate concentrations can be added to achieve rapid staining and clearing in the meanwhile. Through experimental verification, the proposed reagent can perfectly maintain the stability of fluorescence in the samples. We also measured the imaging depth of GFP, PI staining and TH-S staining through experiments, proving the effectiveness of our method. By scanning the porcine brain, we established a sample pretreatment step to prevent the deformation of the sample. At the sectioning layer, the deformation of the sample is only a few micrometers.

In summary, we obtained Aβ plaques distribution in mouse brain and cytoarchitecture data in the porcine hemisphere at cellular resolution using on-line clearing and staining method. By calculating the total time for different samples, it was found that on-line clearing and staining can significantly double imaging system efficiency. However, it should be noted that the 4X objective currently used in our system cannot provide sufficiently detailed images, especially in the axial direction. A higher magnification and large numerical aperture objective require longer imaging time, while on-line clearing and staining method only reduce physical sectioning time and stage movement time. Therefore, for submicron high-resolution imaging system, on-line clearing and staining method maybe not significantly shorten the total time. In addition, processing the massive data generated in 3D imaging of large volume samples poses a huge challenge for the research and analysis of biological problems [39]. Image enhancement and extracting valuable information from massive data using deep learning is a feasible solution [40]. In short, on-line clearing and staining can obtain cellular resolution datasets of large volume sample at high speed. By analyzing and researching on the brain of large mammals, it has the potential to uncover more biological mysteries and help humans overcome various diseases.

Disclosures. The authors declare that there are no conflicts of interest related to this article.

Data availability. Data underlying the results presented in this paper are not publicly available at this time but maybe obtained from the authors upon reasonable request.

Reference

1. J. Defelipe, "The evolution of the brain, the human nature of cortical circuits, and intellectual creativity," Front. Neuroanat. **5**, 29 (2011).
2. J. W. Lichtman and W. Denk, "The big and the small: challenges of imaging the brain's circuits," Science **334**(6056), 618–623 (2011).
3. A. T. Eggebrecht, S. L. Ferradal, A. Robichaux-Viehoever, M. S. Hassanpour, H. Dehghani, A. Z. Snyder, T. Hershey, and J. P. Culver, "Mapping distributed brain function and networks with diffuse optical tomography," Nat. Photonics **8**(6), 448–454 (2014).
4. N. G. Horton, K. Wang, D. Kobat, C. G. Clark, F. W. Wise, C. B. Schaffer, and C. Xu, "In vivo three-photon microscopy of subcortical structures within an intact mouse brain," Nat. Photonics **7**(3), 205–209 (2013).
5. M. B. Ahrens, M. B. Orger, D. N. Robson, J. M. Li, and P. J. Keller, "Whole-brain functional imaging at cellular resolution using light-sheet microscopy," Nat. Methods **10**(5), 413–420 (2013).
6. H. U. Dodt, U. Leischner, A. Schierloh, N. Jahrling, C. P. Mauch, K. Deininger, J. M. Deussing, M. Eder, W. Zieglgansberger, and K. Becker, "Ultramicroscopy: three-dimensional visualization of neuronal networks in the whole mouse brain," Nat. Methods **4**(4), 331–336 (2007).
7. H. Hama, H. Kurokawa, H. Kawano, R. Ando, T. Shimogori, H. Noda, K. Fukami, A. Sakaue-Sawano, and A. Miyawaki, "Scale: A chemical approach for fluorescence imaging and reconstruction of transparent mouse brain," Nat. Neurosci. **14**(11), 1481–1488 (2011).
8. M. T. Ke, S. Fujimoto, and T. Imai, "SeeDB: A simple and morphology-preserving optical clearing agent for neuronal circuit reconstruction," Nat. Neurosci. **16**(8), 1154–1161 (2013).
9. A. Ertürk, K. Becker, N. Jährling, C. P. Mauch, C. D. Hojer, J. G. Egen, F. Hellal, F. Bradke, M. Sheng, and H. U. Dodt, "Three-dimensional imaging of solvent-cleared organs using 3DISCO," Nat. Protocols **7**(11), 1983–1995 (2012).
10. K. Chung and K. Deisseroth, "CLARITY for mapping the nervous system," Nat. Methods **10**(6), 508–513 (2013).

11. E. A. Susaki, K. Tainaka, D. Perrin, F. Kishino, T. Tawara, T. M. Watanabe, C. Yokoyama, H. Onoe, M. Eguchi, S. Yamaguchi, T. Abe, H. Kiyonari, Y. Shimizu, A. Miyawaki, H. Yokota, and H. R. Ueda, "Whole-brain imaging with single-cell resolution using chemical cocktails and computational analysis," Cell **157**(3), 726–739 (2014).

12. B. Hou, D. Zhang, S. Zhao, M. Wei, Z. Yang, S. Wang, J. Wang, X. Zhang, B. Liu, L. Fan, Y. Li, Z. Qiu, C. Zhang, and T. Jiang, "Scalable and DiI-compatible optical clearance of the mammalian brain," Front. Neuroanat. **9**, 19 (2015).

13. D. Jing, S. Zhang, W. Luo, X. Gao, Y. Men, C. Ma, X. Liu, Y. Yi, A. Bugde, B. Zhou, Z. Zhao, Q. Yuan, J. Feng, L. Gao, W. Ge, and H. Zhao, "Tissue clearing of both hard and soft tissue organs with the PEGASOS method," Cell Res. **28**(8), 803–818 (2018).

14. J Zhu, T Yu, Y Li, J Xu, Y Qi, Y Yao, Y Ma, P Wan, Z Chen, X Li, H Gong, Q Luo, and D Zhu, "MACS: rapid aqueous clearing system for 3D mapping of intact organs," Adv. Sci. **7**(8), 1903185 (2020).

15. C. Pan, R. Cai, F. P. Quacquarelli, A. Ghasemigharagoz, A. Lourbopoulos, P. Matryba, N. Plesnila, M. Dichgans, F. Hellal, and A. Ertürk, "Shrinkage-mediated imaging of entire organs and organisms using uDISCO," Nat. Methods **13**(10), 859–867 (2016).

16. K. Matsumoto, T. T. Mitani, S. A. Horiguchi, J. Kaneshiro, T. C. Murakami, T. Mano, H. Fujishima, A. Konno, T. M. Watanabe, H. Hirai, and H. R. Ueda, "Advanced CUBIC tissue clearing for whole-organ cell profiling," Nat. Protocols **14**(12), 3506–3537 (2019).

17. R. Cai, C. Pan, and A. Ghasemigharagoz, *et al.*, "Panoptic imaging of transparent mice reveals whole-body neuronal projections and skull–meninges connections," Nat. Neurosci. **22**(2), 317–327 (2019).

18. V. Nudell, Y. Wang, Z. Pang, N. K. Lal, M. Huang, N. Shaabani, W. Kanim, J. Teijaro, A. Maximov, and L. Ye, "HYBRiD: hydrogel-reinforced DISCO for clearing mammalian bodies," Nat. Methods **19**(4), 479–485 (2022).

19. X. Yang, T. Jiang, L. Liu, X. Zhao, X. Yu, M. Yang, G. Liu, and Q. Luo, "Observing single cells in whole organs with optical imaging," J. Innov. Opt. Health Sci. **16**(01), 2230011 (2023).

20. A. Li, H. Gong, B. Zhang, Q. Wang, C. Yan, J. Wu, Q. Liu, S. Zeng, and Q. Luo, "Micro-optical sectioning tomography to obtain a high-resolution atlas of the mouse brain," Science **330**(6009), 1404–1408 (2010).

21. M. N. Economo, N. G. Clack, L. D. Lavis, C. R. Gerfen, K. Svoboda, E. W. Myers, and J. Chandrashekar, "A platform for brain-wide imaging and reconstruction of individual neurons," eLife **5**, e10566 (2016).

22. K. Seiriki, A. Kasai, and T. Hashimoto, *et al.*, "High-speed and scalable whole-brain imaging in rodents and primates," Neuron **94**(6), 1085–1100 (2017).

23. Q. Zhong, A. Li, R. Jin, D. Zhang, X. Li, X. Jia, Z. Ding, P. Luo, C. Zhou, C. Jiang, Z. Feng, Z. Zhang, H. Gong, J. Yuan, and Q. Luo, "High-definition imaging using line-illumination modulation microscopy," Nat. Methods **18**(3), 309–315 (2021).

24. H. Gong, D. Xu, J. Yuan, X. Li, C. Guo, J. Peng, Y. Li, L. A. Schwarz, A. Li, B. Hu, B. Xiong, Q. Sun, Y. Zhang, J. Liu, Q. Zhong, T. Xu, S. Zeng, and Q. Luo, "High-throughput dual-colour precision imaging for brainwide connectome with cytoarchitectonic landmarks at the cellular level," Nat. Commun. **7**(1), 12142 (2016).

25. H. Wu, X. Yang, S. Chen, L. Zhang, B. Long, C. Tan, J. Yuan, and H. Gong, "On-line optical clearing method for whole-brain imaging in mice," Biomed. Opt. Express **10**(5), 2612–2622 (2019).

26. S. Hildebrand, A. Schueth, A. Herrler, R. Galuske, and A. Roebroeck, "Scalable labeling for cytoarchitectonic characterization of large optically cleared human neocortex samples," Sci. Rep. **9**(1), 10880 (2019).

27. E. A. Susaki, C. Shimizu, and A. Kuno, *et al.*, "Versatile whole-organ/body staining and imaging based on electrolyte-gel properties of biological tissues," Nat. Commun. **11**(1), 1982 (2020).

28. T. Jiang, B. Long, H. Gong, T. Xu, X. Li, Z. Duan, A. Li, L. Deng, Q. Zhong, X. Peng, and J. Yuan, "A platform for efficient identification of molecular phenotypes of brain-wide neural circuits," Sci. Rep. **7**(1), 13891 (2017).

29. T. Yang, T. Zheng, Z. Shang, X. Wang, X. Lv, J. Yuan, and S. Zeng, "Rapid imaging of large tissues using high-resolution stage-scanning microscopy," Biomed. Opt. Express **6**(5), 1867–1875 (2015).

30. S. Karma, J. Homan, C. Stoianovici, and B. Choi, "Enhanced fluorescence imaging with DMSO-mediated optical clearing," J. Innov. Opt. Health Sci. **03**(03), 153–158 (2010).

31. L. Chen, G. Li, Y. Li, Y. Li, H. Zhu, L. Tang, P. French, J. McGinty, and S. Ruan, "UbasM: An effective balanced optical clearing method for intact biomedical imaging," Sci. Rep. **7**(1), 12218 (2017).

32. D. S. Richardson and J. W. Lichtman, "Clarifying tissue clearing," Cell **162**(2), 246–257 (2015).

33. H. Xiong, Z. Zhou, M. Zhu, X. Lv, A. Li, S. Li, L. Li, T. Yang, S. Wang, Z. Yang, T. Xu, Q. Luo, H. Gong, and S. Zeng, "Chemical reactivation of quenched fluorescent protein molecules enables resin-embedded fluorescence microimaging," Nat. Commun. **5**(1), 3992 (2014).

34. S. Preibisch, S. Saalfeld, J. Schindelin, and P. Tomancak, "Software for bead-based registration of selective plane illumination microscopy data," Nat. Methods **7**(6), 418–419 (2010).

35. R. Michael, A. Lenferink, G. F. J. M. Vrensen, E. Gelpi, R. I. Barraquer, and C. Otto, "Hyperspectral Raman imaging of neuritic plaques and neurofibrillary tangles in brain tissue from Alzheimer's disease patients," Sci. Rep. **7**(1), 15603 (2017).

36. R. Guntern, C. Bouras, P. R. Hof, and P. G. Vallet, "An improved thioflavine S method for staining neurofibrillary tangles and senile plaques in Alzheimer's disease," Experientia **48**(1), 8–10 (1992).

37. L. Y. Katherine, L. M. Tai, T. Kanekiyo, W. B. S. Jr, S. Michon, E. Nwabuisi-Heath, A. M. Manelli, Y. Fu, S. Riordan, W. A. Eimer, L. Binder, G. Bu, C. Yu, D. M. Hartley, and M. J. LaDu, "Intraneuronal Aβ detection in 5xFAD mice by a new Aβ-specific antibody," Mol. Neurodegener. **7**(1), 8 (2012).

38. C. Zhou, X. Yang, S. Wu, Q. Zhong, T. Luo, A. Li, G. Liu, Q. Sun, P. Luo, L. Deng, H. Ni, C. Tan, J. Yuan, Q. Luo, X. Hu, X. Li, and H. Gong, "Continuous subcellular resolution three-dimensional imaging on intact macaque brain," Sci. Bull. **67**(1), 85–96 (2022).
39. E. Landhuis, "Neuroscience: Big brain, big data," Nature **541**(7638), 559–561 (2017).
40. Y. Zhang, P. Wu, S. Chen, H. Gong, and X. Yang, "FCE-Net: a fast image contrast enhancement method based on deep learning for biomedical optical images," Biomed. Opt. Express **13**(6), 3521–3534 (2022).